Preprint typeset using LaTeX style emulateapj v. 5/2/11

arXiv:1603.04959v1 [astro-ph.SR] 16 Mar 2016

ON THE BRIGHT LOOP TOP EMISSION IN POST ERUPTION ARCADES

Rohit Sharma[1], Durgesh Tripathi[2], Hiroaki Isobe[3] and Avyarthana Ghosh[2,4]

ABSTRACT

The observations of post eruption arcades (PEAs) in X-rays and EUV reveal strong localised brightenings at the loop top regions. The origin of these brightenings and their dynamics is not well understood to date. Here, we study the dynamics of PEAs using one-dimensional hydrodynamic modelling with the focus on the the understanding of the formation of localised brightening.Our findings suggest that these brightenings are the result of collisions between the counter-streaming chromospheric evaporation from both the foot points. We further perform forward modelling of the emission observed in simulated results in various spectral lines observed by the Extreme-Ultraviolet Imaging Telescope aboard Hinode. The forward modelled intensities in various spectral lines are in close agreement with a flare observed in December 17, 2006 by EIS.

1. INTRODUCTION

Solar flares are possibly the brightest and most energetic bursts occurring in the atmosphere of the Sun. They release the high content of radiation and energetic particles into the interplanetary medium and play a key role in determining space-weather. Our understanding of the physics of solar flares is in a level that there exists the "standard model", in which plasma ejection and magnetic reconnection play key roles (Shibata & Magara 2011), though there still remain many physical processes that are poorly understood. One such challenge is to explain the loop top emission observed in EUV and soft X-ray observations of post flare loops or post eruption arcades (Priest & Forbes 2002), which are considered to be one of the best proxies for Coronal Mass Ejections (CMEs) source regions (Tripathi et al. 2004). However, no one-to-one correlation exists (see e.g., Ma et al. 2010; Howard & Harrison 2013; Chen et al. 2015; Sun et al. 2015).

One of the first observations of loop top emission in soft X-ray images was reported by Acton et al. (1992). Using the data taken from Soft X-ray Telescope (SXT) (Tsuneta et al. 1991) on board Yohkoh for 10 flares, Acton et al. (1992) found presence of compact X-ray sources at the loop tops, which were underneath the cusp-shape structures (Forbes & Acton 1996). Studying the flare that occurred on 13th January 1992, using the observations recorded by Yohkoh SXT and hard X-ray telescope (HXT) (Kosugi et al. 1991; Tsuneta et al. 1991), Masuda et al. (1994) discovered Hard X-ray sources at the loop top as well as the two footpoints of post flare loops. The HXR loop top observed by Masuda et al. (1994) was located at the top of the SXR cusp detected in the SXT images. The presence of cusp, and co-spatial HXR emission was attributed to magnetic reconnection processes (Forbes & Acton 1996; Priest & Forbes 2002). However, there is no consensus on the origin of the soft X-ray and EUV brightening at the loop top.

With the launch of Hinode, it became possible to observe flares across a range of temperatures using the X-Ray Telescope (XRT)and the Extreme-ultraviolet Imaging Spectrometer (EIS). Hara et al. (2008) reported the XRT and EIS observations of a limb flare on December 17, 2006 that show a clear cusp-structure and the loop-top brightening. With the EIS instrument, Hara et al. (2008) could investigate the flare dynamics across a range of temperature. Some iron and calcium spectral lines having formation temperatures from $\log T = 6.0$ to 6.7 is shown in Table 1. In Fig. 1, the panel (a) to (g) shows intensity maps for 6 iron lines Fe X to Fe XV and Ca XVII. In the same figure, the panel (h) shows zoomed maps of loop top region and contours of Fe XV and Fe XII. As can be depicted from the Fig. 1, panel (h) and Table 1, hotter plasma is located at higher coronal heights (i.e., in the outer loops) and cooler plasma is at lower coronal heights (in the inner loops). This is the well-known characteristics since the Yohkoh observations (Tsuneta 1996) that is consistent with the "standard model" with magnetic reconnection (Yokoyama & Shibata 2001). A number of authors have shown that the loop top brightening is not only seen in SXR, but also in EUV observations using narrow band imager (see e.g., Golub et al. 1999; Warren et al. 1999; Warren 2000; Warren & Reeves 2001; Warren & Doschek 2006) obtained by the Transition Region and Coronal Explorer (TRACE; Handy et al. 1999). However, Hara et al. (2008), for the first time made a clear distinction using the spectroscopic observations by Hinode/EIS.

There have been numerous attempts to explain the above described phenomenon using various approaches such as hydrodynamic modelling of multiple loops (Hori et al. 1997), 1-D hydrodynamic modelling in soft X-ray and EUV for SXT and TRACE respectively (Reeves et al. 2007) and retracting loops forming gas-dynamic shock (Longcope et al. 2009; Longcope & Guidoni 2011). However, there is no consensus on the reason behind the observed loop top brightenings in SXR and EUV.

The loop top brightening can be quantified by taking the ratios of the intensities at the loop top region and arm regions of the coronal loop shown in the green boxes

[1] National Centre for Radio Astrophysics, Post Bag 4, Ganeshkhind, Pune 411007, India
[2] Inter-University Centre for Astronomy and Astrophysics, Post Bag 4, Ganeshkhind, Pune 411007, India
[3] Graduate School of Advanced Integrated Studies in Human Survivability, Kyoto University, 1 Yoshida-Nakaadachi-cho, Sakyo-ku, Kyoto 603-8306, Japan
[4] IISER-Kolkata, Mohanpur - 741246, West Bengal, India

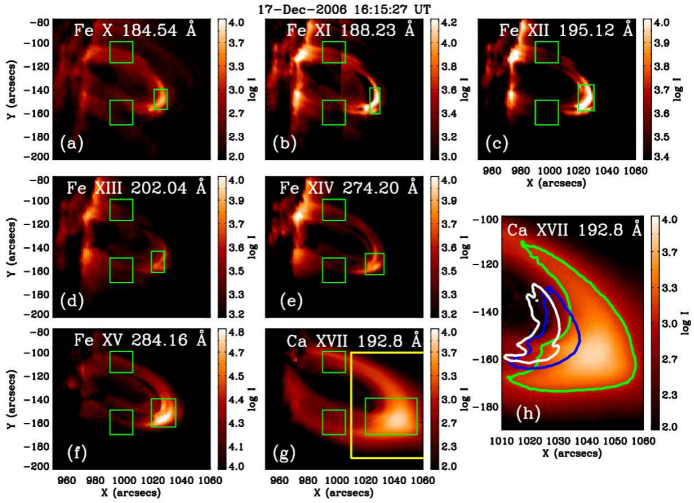

FIG. 1.— Intensity maps (a) to (g) for various spectral lines shown in Table 1. The green boxes shows the area taken for the calculation of parameter brightening factor. Panel (h) is a zoom of yellow box of the Ca XVII map panel (g). The Intensity contours in panel (h) are Ca XVII (thick green), Fe XV (blue) and Fe XII (white). Note that the contours are at 7% level of the maximum intensity in respective lines.

in Fig. 1 and is called brightening factor (β_{obs}). The intensity in the arm regions is calculated by averaging over two coronal arm regions (Fig. 1). Table 1 shows the intensity values and β_{obs} at the loop top for various spectral lines. β_{obs} varies in the range of 1.5 to 3.7. Note that the Fe XV is the brightest spectral line.

In order to explain the bright knots observed in EUV post flares loops with various instruments (Cheng et al. 1980; Dere et al. 1997; Widing & Hiei 1984; Golub et al. 1999; Warren 2000), Patsourakos et al. (2004) performed a 1D hydrodynamic modelling, similar to the calculations performed by Antiochos (1980). It was found that the formation of these bright knots can be explained by spatially localised heating that may be occurring during the decay phase of the flares rather than spatially uniform heating.

In this study, we take a similar approach to study the evolution of the loop top emission in post flare loops observed in soft X-ray and EUV observations. We further perform forward modelling and compare our simulation results with observations provided by EIS for the flare that was studied by Hara et al. (2008). The rest of the paper is structures as follows. The § 2 we provide the details of the numerical model along with initial and boundary conditions. The section § 3 summarises the simulation results. The role of energetics and evolution of density, temperature and velocity is discussed for various heating inputs. Next § 4, deals with the forward modelling of the loop tops in EIS spectral wavebands. Lastly § 5, discusses the results and conclusions.

2. NUMERICAL MODEL

We simplify the problem to one dimensional hydrodynamics of a semi-circular loop with constant cross section as shown in Figure 2. To make the simulation results observationally more viable, we have taken the parameters such as length, approximate energy deposition based on the parameters measured for the C-class flare observed on 17th December 2006, which was studied by Hara et al. (2008). The length of the loop is $\sim$ 180 Mm.

TABLE 1
THE OBSERVATION PARAMETERS FOR VARIOUS SPECTRAL LINES FOR 17TH DECEMBER 2006 FLARE.

Spectral lines	Wavelength (in Å)	Peak (log T)	Loop top Intensity (ergs/cm^2/sec/str)	Brightening factor (β_{obs})
Fe X	184.54	6.00	5.1×10^3	3.67
Fe XI	188.23	6.08	2.6×10^4	2.32
Fe XII	195.12	6.10	1.2×10^4	2.91
Fe XIII	202.04	6.15	5.7×10^3	1.54
Fe XIV	274.2	6.25	7.6×10^3	1.65
Fe XV	284.16	6.30	6.5×10^4	2.18
Ca XVII	192.82	6.70	6.8×10^3	2.70

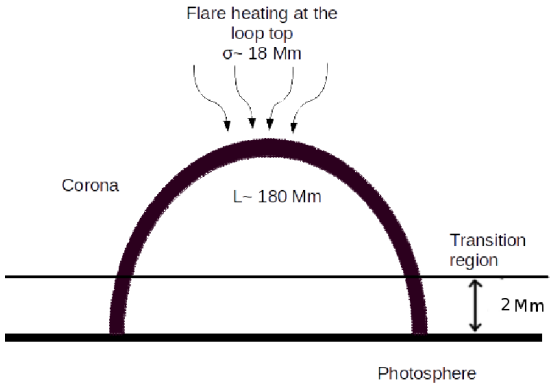

FIG. 2.— Schematic of the 1-D coronal loop, indicating the location of localised flare heating. The total length of the loop (L) is 180 Mm. The transition region location is kept at 2 Mm.

In this simulations we solve the standard hydrodynamic equations, which are described in Equations 1, 2 & 3 with an equation of state of ideal gas in c.g.s units.

$$\frac{\partial \rho}{\partial t} + \frac{\partial}{\partial s}(\rho v) = 0 \quad (1)$$

$$\frac{\partial}{\partial t}(\rho v) + \frac{\partial}{\partial s}(\rho v^2) = -\rho g_{||} - \frac{\partial P}{\partial s} \quad (2)$$

$$\frac{\partial E}{\partial t} + \frac{\partial}{\partial s}[(E+P)v] + \rho g_{||} v = \frac{\partial}{\partial s}(\kappa_{||}\frac{\partial T}{\partial s}) - R + H \quad (3)$$

where,

$$P = n k_B T \quad (4)$$

$$E = \frac{1}{2}\rho v^2 + \frac{P}{\gamma - 1} \quad (5)$$

Here ρ is the total mass density, v is the fluid velocity, P is the total gas pressure, E is the sum of the kinetic energy and the internal energy per unit volume, T is the plasma temperature and s is the length along the loop from the left footpoint. We have assumed a monoatomic ideal gas with specific heat capacity $\gamma = 5/3$. The gravity $g_{||}$ is $g_o\ cos(\frac{h}{r})$, where h is the height from the photosphere, r is the radius of curvature of the loop and g_o is 2.7×10^4 cm/sec^2.

The heat conduction is governed by temperature gradients across the loop with Spitzer conductivity given by

$$\kappa_{||} = \kappa_0 T^{5/2} \quad (6)$$

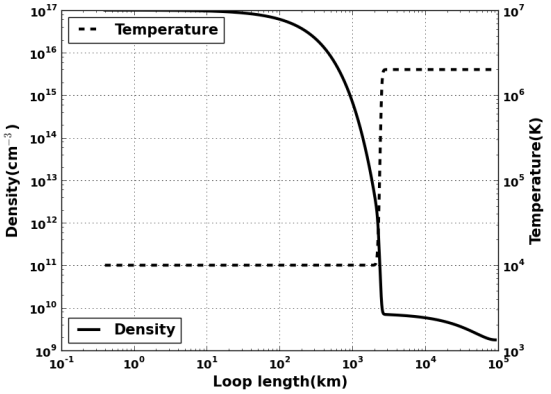

FIG. 3.— Initial temperature and density profiles for the half loop.

where $\kappa_0 = 9\times\ 10^{-7}$. Note that all the units here are in CGS.

In equation 3, H is a heating function *H(s, t)* that consists of a static heating H_s and an flare heating term H_f. The functional form of H is given as:

$$H(s,t) = H_s(s) + H_f(s,t) \tag{7}$$

The static heating is kept constant to maintain the corona at 2 MK. The flare heating term provides the heating due to flare to which the plasma responds and produces the dynamics in the loop. The functional form of the flare heating is given by Equation 8. In this study we have considered the flare heating to have a Gaussian shape with a width of $\sigma \sim 18$ Mm. The mean of the Gaussian is placed at the loop top $s_{top} \sim 90$ Mm.

$$H_f(s,t) = q(t)\frac{H_o}{\sqrt{2\pi}\sigma} exp\Big(- \frac{(s-s_{top})^2}{2\sigma^2}\Big)\ (ergs\ cm^{-2}) \tag{8}$$

where q(t) is the binary switch for the flare heating, i.e., if q(t) is 0 then heating is off and if 1 then heating is on. H_o defines the heating strength, which is kept as a variable. By varying H_o, we can study the dynamics of plasma in flare loops with varying heating strengths.

R in Eqn. 3 is the radiative cooling, which is defined as

$$R(s,t) = \frac{1}{2}\ n_e^2\ Q(T) \tag{9}$$

where $Q(T)$ is the radiative loss function for optically thin plasma and is approximated through various power law functions in different temperature bands in the format $Q(T) = \chi\ T^{\alpha}\ (ergs\ s^{-1}\ cm^{-3})$ and taken directly from Hori et al. (1997).

Figure 3 shows the initial conditions for our simulation. We have started the simulations with realistic initial conditions in terms of temperature and density profile for the solar atmosphere. The system is set up in such as way that the loop is in hydrostatic equilibrium, i.e., static heating fully compensate the radiative cooling energy. The initial temperature is kept at 2 MK because we are mostly interested in active region post flare loops which are best seen in Fe XII lines forming at 2 MK. The density is then computed along the loop using the equations of hydrostatic equilibrium.

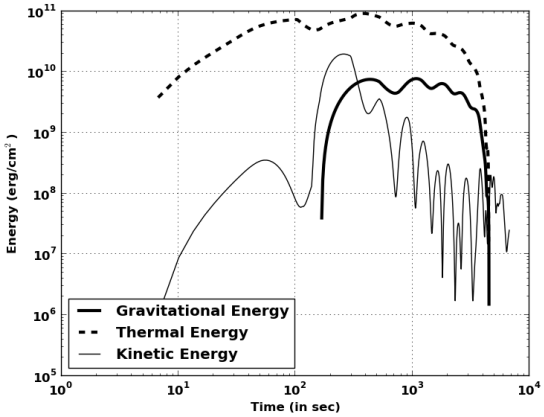

FIG. 4.— Comparison of the different energies in the corona with time. The gravitational(ΔE_{GE}) and thermal energy(ΔE_{TE}) shown is the variation from intial gravitational and thermal energy of the loop respectively.

We have also considered the loop to be symmetric across its length. Considering this geometry leads us to solve the equations only for half of the loop (from one footpoint to the loop top). The solution of the other part will then become the mirror image. The boundary conditions are set up so that there are no gradient in temperature and density at the loop top. Mathematically the boundary condition can be written as $(\frac{\partial n}{\partial s})_{top} = 0$, $(\frac{\partial T}{\partial s})_{top} = 0$ and $v_{top} = 0$.

3. RESULTS

3.1. *Overview*

We have performed simulations for six different external heating (H_f) applied at the loop top. The heating input to the loop will be 2×10^9, 2×10^{10}, 4×10^{10}, 8×10^{10}, 1.2×10^{11}, 2.0×10^{11} ergs cm^{-2} uniformly in a time of 100 sec each. These energy values corresponds to the energy of a C-class flare ($\sim 10^{29}$ ergs) distributed over 18 Mm length. We note that the flare observed by Hara et al. (2008) is a C-class flare. A few different values of heating strengths are chosen so as to cover two orders of magnitude centring at C-class flares strengths.

One of the first parameters which needs to be verified is the principle of energy conservation throughout the simulations. We note that before the deposition of any external heat, the system is in hydrostatic equilibrium i.e. the static heating in the system balances out the radiative cooling. After the heat deposition, we have carefully looked at the different form of energy available in system and their evolution.

First we discuss the energetics and dynamics of the loop evolution for the highest heating case i.e. 2.0×10^{11} ergs cm^{-2} in detail. We note that same line of arguments will follow for the other heating scenarios. We calculate total thermal (E_{TE}), kinetic (E_{KE}) and gravitational energy (E_{GE}) in the corona. The coronal part of the loop is defined as the portion of the loop above than 2 Mm. Figure 4 shows the temporal evolution of the changes in the total thermal energy (ΔE_{TE}), total kinetic energy (ΔE_{KE}) and total gravitational energy (ΔE_{GE}) in the coronal part of the loop with respect to that at t=0. For energy component E, $\Delta E = E(t) - E(t=0)$. There is no total kinetic energy in the loop at t=0 as $v(s) = 0$, so $\Delta E_{KE} = E_{KE}$.

As can be seen from the Figure 4, the thermal energy (ΔE_{TE}) starts to increase and attains a maximum at time ∼100 sec. This is consistent with fact that the external heat was supplied only for the first 100 sec. Thereafter, the thermal energy (ΔE_{TE}) shows small fluctuations ∼ 10% and declines sharply after ∼ 4000 sec. Similarly, kinetic energy(ΔE_{KE}) also increases and attains a maximum at around ∼60 sec. It reaches minima at time ∼ 102 sec and rises sharply reaching second maxima at time ∼ 300 sec. Thereafter kinetic energy fluctuates and the level of fluctuation in the kinetic energy is ∼ 50%. Also, ΔE_{GE} is nil for first 100 sec. It starts to increase sharply at ∼105 sec and attains a maximum at 300 sec and later fluctuate at ∼ 10% level. Afterwards, it falls sharply at around ∼ 3500 sec.

Figure 5 plots the time evolution of density (panel a), temperature (panel b), velocity (panel c) and pressure(panel d). Note that the plots display the above said parameters only for the half of the loop. The initial profile for all parameters is plotted at t=0. At t=40 sec, the temperature (Fig. 5, panel (b)) of the loop top rises to 10 MK and temperature profiles develops a spatially broader profile. The velocity profile (Fig. 5, panel (c)) is roughly uniformly negative in higher corona from 25 Mm to 80 Mm and shows small bump near length ∼ 8 Mm.

At t = 132 sec, the coronal temperature profile flattens to ∼ 10 MK. The velocity profile develops strong positive profile reaching speeds of 200 km sec^{-1}. The density develops a steep gradient near 20 Mm and pressure profile now shows a negative dip near the same location. Since the flare heating stops at t=100 s, the coronal temperature dips (t=306 s, panel(b)). At 306 sec, the density and pressure profiles (Fig. 5, panel (a) & (d)) shows a sharp increase at the loop top and velocity (panel(c)) shows large positive profile near loop top at length ∼88 Mm. The sharp enhancement in density propagate towards bottom of the loop (Fig. 5, panel (a) & (d), t=476 s) with a velocity (panel(c), t=476 s) of 120 km/sec. At very large times t = 2040 sec, the loop cools down to few million K. However, the density and pressure profiles quietens and settles. The velocity profile becomes spatially flatter and negative.

The evolution of energy shown in Figure 4 as well as the other physical parameters shown in Figure 5 can be described as follows. As can be seen in Figure 5 panel b, the external heat input increases the temperature (broader bump at t=40 s), that in turn increases the thermal energy that is reflected in Figure 4 (dashed line). The increase in thermal energy(ΔE_{TE}) creates a pressure gradient from the loop top to the loop bottom (see panel d, t=40 s) that invokes a downward velocity flow or conduction front (from loop top to loop footpoint) with a speed of 42 km/sec uniformly throughout the corona as shown in panel c (t=40 s). Here, we describe negative velocity as the flow from top to bottom. Due to the downflowing plasma, the kinetic energy(ΔE_{KE}) in system increases, which is also reflected in Figure 4 (thin solid line).

The downward conduction front (downflow) produced due to the pressure gradient hits the chromosphere at ∼120-130 sec and produces fast upflows (see Fig. 5 panel c t=132 sec), a phenomena known as "chromospheric evaporation". Due to the chromospheric evaporation, the thermal energy(ΔE_{TE}), kinetic energy(ΔE_{KE}), as well as the gravitational (ΔE_{GE}) show an increase. The velocity of the chromospheric evaporation reaches up to ∼220 km sec^{-1}. Since the loop is considered to be symmetric and external heat input is at the center of the loop, the evaporation flow has the same speed from both the foot points. The evaporation flows from the two points collide at the loop top. We refer to it as primary collision of the evaporation flow and it leads to a sharp increment in density at loop top (see Fig. 5 (a) t=306 sec) as well as thermal energy (see Figure 4 dashed line). After the primary collision, the mean kinetic energy(ΔE_{KE}) starts to decline and show oscillatory behaviour. This is suggestive of the fact that there may be secondary, tertiary multiple downflows and upflows. The gravitational energy(ΔE_{GE}), however, remains rather constant until t=3500 sec, suggesting no significant movement of matter. Therefore, it is plausible to conclude that the secondary and other downflows/upflows replicated in kinetic energy curve in Fig. 4 are weak.

TABLE 2
Loop top parameters at the time of primary shock collision for various heating strengths. NOTE: The Mach number is calculated adjacent to the loop top.

$H_f \times 10^9$ (ergs cm^{-2})	Factor of Increment (δ)	Coronal density ($\times 10^8$ cm^{-3})	$\mathbf{T}_{top}$ (MK)	M_a
2.0	1.21	1.52	1.97	0.24
20.0	1.35	2.32	3.49	0.33
40.0	1.36	2.48	4.73	0.39
80.0	1.69	3.98	6.48	0.60
120.0	1.86	4.15	7.61	0.63
200.0	2.17	4.32	9.43	0.62

At later times (∼ 2000 sec and afterwards), the density in the corona of the loop is uniformly higher compared to initial density profile by a factor of 3. The gravitational energy (ΔE_{GE}) remains flat till 2000 sec with very small variation (see Fig. 4). Both the thermal energy (ΔE_{TE}) as well as gravitational energy(ΔE_{GE}) show steep decline afterwards. This is suggestive of strong cooling and draining of plasma from the corona to the chromosphere.

3.2. *Dynamics of the loop for various input heats*

The time evolution of density and temperature along the loop for different heating strengths is shown in Figures 6 & 7. The time steps shown are chosen so as to describe the collision of primary evaporation at the loop top. The strength of externally supplied heat is given in the figure. As can be clearly seen in the density plots of Fig. 6 7, the primary flow collision creates an enhancement in density at the loop top. With the increasing strength of external heat, the enhancement in density increases and starts to appear at earlier times. The temperature profile of the corona increases uniformly for large heating inputs. To make a quantitative assessment in the changes in density and temperature with increasing heat input, we have defined a parameter "density increment factor" (δ) as the ratio of the loop top density after the collision to the ambient coronal density. The variation of δ and loop top temperature with increasing external heat input is given in Table 2. The table clearly reveals that density increment factor δ as well as the loop top temperature increases with the increasing strength of external heat input. We also calculate the Mach number very close to the loop top just after the collision. For all heating strengths the primary collision remains subsonic.

The increase in density and temperature at loop tops

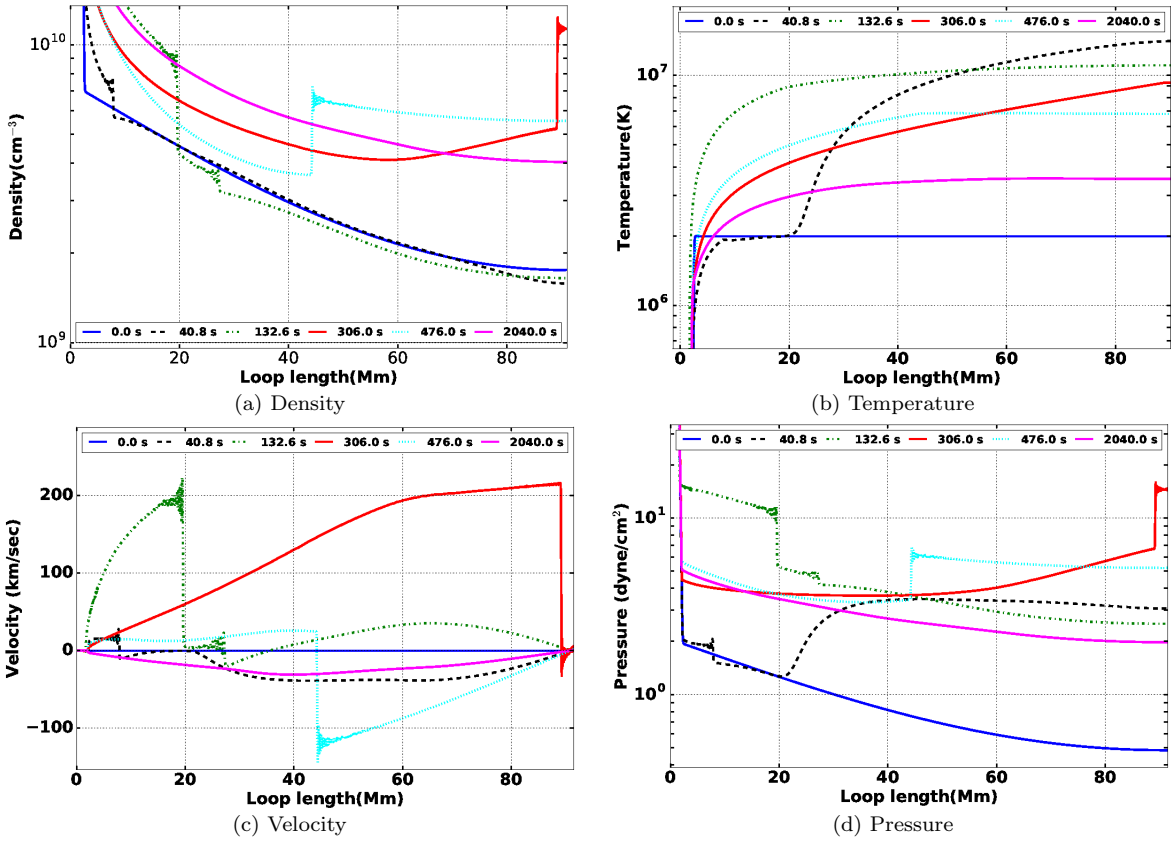

(a) Density (b) Temperature (c) Velocity (d) Pressure

FIG. 5.— The panel shows the plots of density, temperature, velocity and pressure at various times for input heating of 2×11^{10} ergs cm^{-2}.

with increasing external heat input can be explained as following. The stronger heat input creates stronger conduction front from loop top towards the footpoint and dumps larger matter and energy in the chromosphere. This leads to a stronger evaporation flow. In all the case, the coronal temperature increases till the first 100 seconds corresponding to the heat input time and then drops as the loop cools. Later on, the coronal part of the loop near the loop top show an enhancement in the temperature which corresponds to the time of the primary collision of the evaporation flow. This temperature enhancement is strongly related to enhancement in the density (see Figures. 6 & 7). After the collision of the primary chromospheric evaporation flow, the reverse flow is created that moves towards chromosphere and collides with secondary and tertiary flows coming from the chromospheric regions to coronal region. These flow collisions occur at various places in the loop depending on the flow speeds. However, these collisions are weak and the temperature and density increment is less compared to the primary collision at the loop top. We expect subsequent reverse flow collisions to be strong for asymmetric heating cases. It may explain the observation of knots seen in EUV observations and modelled by Patsourakos et al. (2004).

4. FORWARD MODELLING OF SPECTRAL LINES OBSERVED WITH EIS

The enhancement in the loop top density and temperature is expected to get reflected in various coronal emission lines. In this section, we forward model various spectral lines observed by EIS covering a range of peak formation temperature of 1.0 to 5.6 MK. The spectral lines which are forward modelled and their peak formation temperature is given in Table 3. The peak formation temperature and other atomic parameters are obtained from CHIANTI v.7.0 (Dere et al. 1997; Landi et al. 2013).

TABLE 3
THE EIS SPECTRAL LINES CHOSEN FOR FORWARD MODELLING

Ionised State	Wavelength($\AA$)	Peak Formation Temperature (MK)
Fe X	184.54	1.1
Fe XI	188.23	1.4
Fe XII	195.19	1.6
Fe XV	284.16	2.2
Ca XVII	192.8	5.6

Intensity of an optical thin emission line can be written as,

$$I_{i,j}(\nu) = \int G_{ji}(T_e, n_e) n_e^2 dl \qquad (10)$$

where i,j are upper and lower levels respectively. G(T_e,n_e) is the contribution function of the spectral line that accounts for the ionisation fraction, coronal abundances (A_X). It has strong depends on electron temperature. The expression of G(T_e,n_e) is given by,

$$G_{ji}(T, n_e) = \frac{hc}{4\pi\lambda_{ji}} \frac{A_{ji}}{n_e} \frac{N_j(X^{+k})}{N(X^{+k})} \frac{N(X^{+k})}{N(X)} A_X \qquad (11)$$

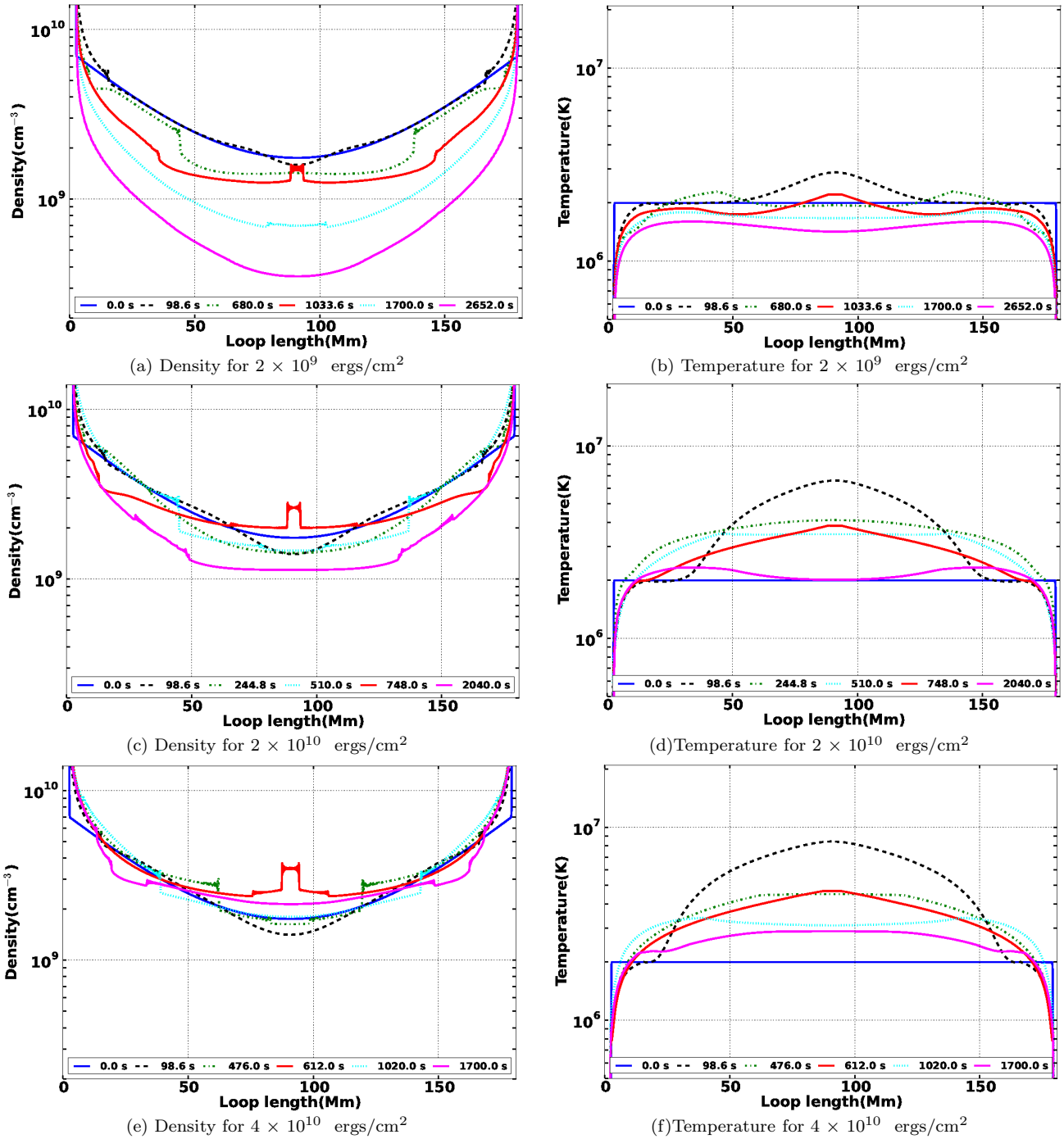

(a) Density for 2×10^9 ergs/cm^2

(b) Temperature for 2×10^9 ergs/cm^2

(c) Density for 2×10^{10} ergs/cm^2

(d)Temperature for 2×10^{10} ergs/cm^2

(e) Density for 4×10^{10} ergs/cm^2

(f)Temperature for 4×10^{10} ergs/cm^2

FIG. 6.— Density and Temperature evolution for various heating strengths.

where A_{ij} is the spontaneous transition probability for j to i transition. $\frac{N_j(X^{+k})}{N(X^{+k})}$ is the population of level j relative to the total $N(X^{+k})$ number density of ion X^{+k}. $N(X^{+k})$ and $N(X)$ are the element species in k^{th} ionised state and neutral state respectively.

We have computed the contribution function for each spectral lines using CHIANTI for a given electron density and coronal abundances of Feldman (1992). Note that, in this study we are only forward modelling the spectral lines (given in Table 3) which are not density sensitive. The contribution functions for all the lines listed in Table 3 are plotted in Figure 8.

We have forward modelled the loop intensities in all the spectral lines listed in Table 3 using the density and temperatures obtained at each point along the loop. We note that the forward modelling was only performed to the coronal part of the loop. This is essentially due to the fact that the assumption of optically thin atmosphere will breakdown near the footpoint of the loop in the chromosphere.

Figure 9 displays the evolution of the intensities in

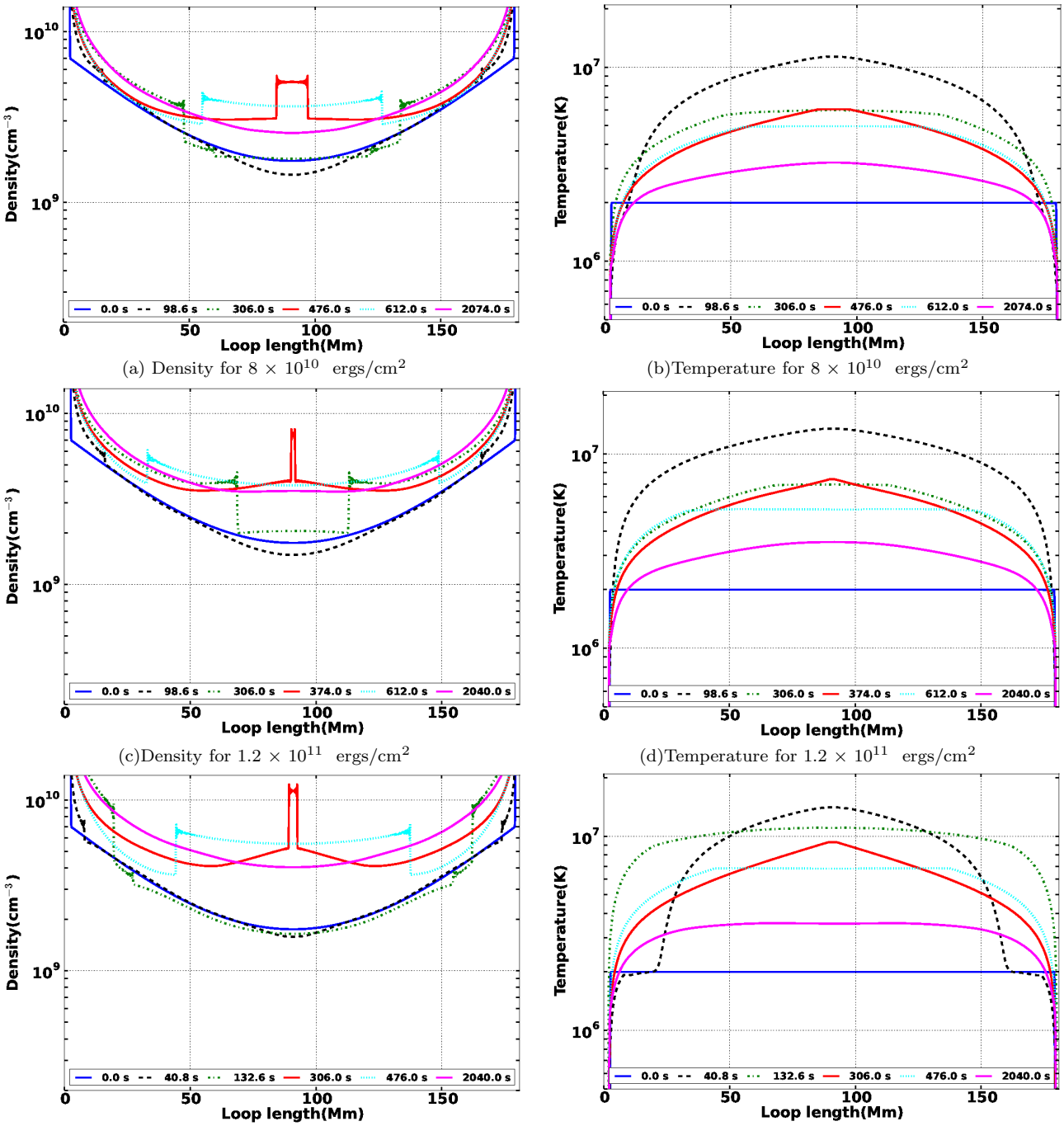

(a) Density for 8×10^{10} ergs/cm^2

(b)Temperature for 8×10^{10} ergs/cm^2

(c)Density for 1.2×10^{11} ergs/cm^2

(d)Temperature for 1.2×10^{11} ergs/cm^2

(e)Density for 2×10^{11} ergs/cm^2

(f)Temperature for 2×10^{11} ergs/cm^2

FIG. 7.— Density and Temperature evolution for various heating strengths.

these spectral lines at the loop top for the highest heating scenario. In the figure, the bold solid black line corresponds to the temperature at the top, dashed-dotted green line is intensity of Fe XV line, the dashed blue line is the intensity of Ca XVII line, dotted red line is the intensity of Fe XII, thin solid yellow line is the intensity of Fe XI and thick dashed magenta line is the intensity of Fe X line. The temperature at the loop top show increase till 100 sec, reflecting the time till which the external heating was switched-on and decreases afterwards.

At initial times (t $\sim$ 3.4 sec), where the temperature is T $\sim$ 6.48 MK, the intensity of Fe XV and Ca XVII are almost the same. As we see from Figure 8, coincidently, the contribution functions of these two lines cross each other exactly at the temperature T = 6.48 MK that can explain the equal intensity. This temperature nearly corresponds to the peak of the contribution function of Ca XVII and lies in the far right side of that of Fe XV. With the increase of temperature, the intensities in both the spectral lines fall. The emission in Fe XV completely disappears when the temperature reaches to roughly 12 MK, as this line has contribution function, al-

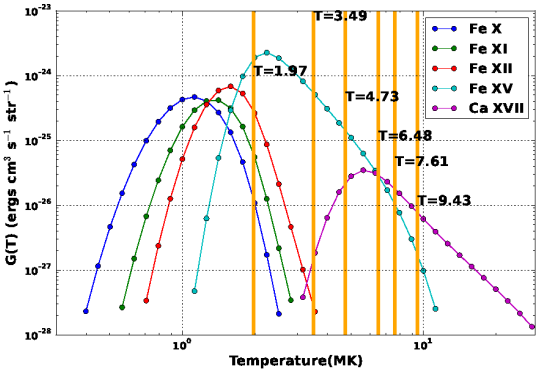

FIG. 8.— Contribution function of the spectral lines listed in Table 3 computed using a density of 10^9 cm^{-3} and coronal abundances of Feldman et al. 1992 and CHIANTI. The orange lines corresponds to the loop top temperature (in MK) at the time of collision of primary flows corresponding to the six simulations with varying heart strength. The temperature increased from $T = 1.97$ MK to $T = 9.43$ MK corresponding to increasing heating strength.

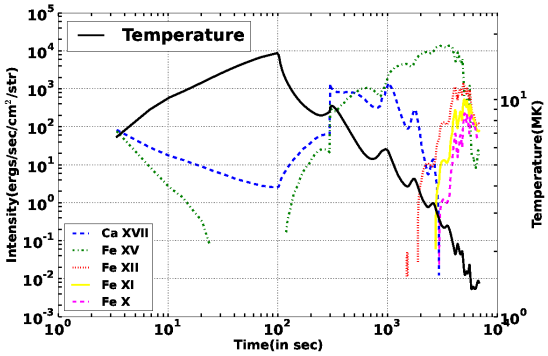

FIG. 9.— The figure plots spectral line intensities and temperature of the loop top for external heating input of 2×10^{11} ergs cm^{-2}. The bold solid line correspond to the temperature, dashed-dotted line is intensity of Fe XV lines, the dashed line is the intensity of Ca XVII line, dotted line is the intensity of Fe XII, thin solid line is the intensity of Fe XI and thick dashed line is the intensity of Fe X.

beit very minimal, reaching to a maximum temperature of 10 MK. The intensity in Ca XVII also decreases but never disappears as the contribution function of this line goes as large as $\sim$ 12 MK.

After 100 seconds, i.e., when the external heating is switched-off, the loop top starts to cool and the intensity in Ca XVII starts to increase, as we move towards the peak of it's contribution function. The emission from Fe XV also reappears, albeit later (at t= 101 sec). At t=300 sec, the temperature show a slight enhancement due to the primary collision of the evaporation flow (as explained in 3.2 and shown Figure 7). Correspondingly, the intensities in Fe XV and Ca XVII show a slight dip followed by a very sharp increase, which is about two orders of magnitude higher. This sharp enhancement in the intensities coincide with the time of the collision of the primary evaporation flow collision as well as the enhancement in the density. Later on, the temperature falls and shows many bumps before it dies out. The intensity in Ca XVII remains similar with some fluctuations till t=1000 s and falls sharply afterwards. Whereas, the intensity of Fe XV keeps increasing with oscillations all the way till t=3000 s that corresponds to a temperature of 3 MK. The oscillations in the intensities of Ca XVII as well as in Fe XV corresponds well to the times of bumps see the temperature profile. These oscillations are essentially due to the collisions of the subsequent evaporation flows. The fall of intensities of these two lines corresponds to the cool-ward fall of their contribution function. The spectral lines Fe XII, Fe XI and Fe X appears at times t=1040, 1150, 1180 sec respectively and they do not fade away till the end of simulation. As the loop cools, the other spectral lines gain in the contribution function and results in the enhancement in their intensities. Also note that the appearance of Fe XII preceded that of Fe X appears, which can be attributed to their corresponding contribution function.

After the primary collision (t=304 sec), the dips in the temperature correlates with the peaks in the intensities of Fe XV, Fe XII, Fe XI and Fe X. Whereas, reverse is true for Ca XVII as temperature dips correlates with the Ca XVII intensity dips. This is essentially due to the fact that the temperature of the loop top is less than 5.6 MK (peak formation temperature of Ca XVII) and it falls on the positive slope of the contribution function of Ca XVII and negative slope of that of Fe XV, Fe XII, Fe XI and Fe X lines (see Figure 8). If temperature lies in negative slope in G(T) curve, any increase in the temperature should show decreases in the intensities of these lines and vice versa. However, we can see in Figures 6 and 7 , the collision of evaporation flows also enhances the densities that could in turn enhance the emission measure thereby showing the increase in the intensities. The factor of increment of densities δ for this largest heating case is 2.17 seen in Table 2.

Figure 10 displays the evolution of intensities at the loop top for different heating strengths. In the figure, the bold black solid line correspond to the temperature of the top, dashed-dotted green line is intensity of Fe XV lines, the dashed blue line is the intensity of Ca XVII line, dotted red line is the intensity of Fe XII, thin solid yellow line is the intensity of Fe XI and thick dashed magenta line is the intensity of Fe X. While explaining the evolution of loop top emission in various lines, similar argument will follow as is given earlier for the highest heating case. As we can see, the appearance and disappearance of the emission in various spectral lines corresponds well with their respective contribution functions. For example, for the lowest heating case, the emission in Ca XVII appears for a very short duration, only at the time of peak temperature achieved during heating. Afterwards, the emission on Ca XVII dies down. Similarly, the Fe X line appears strongly for the lower heating case much earlier than it appears in the higher heating case (see Figure 10).

We have provided the density increment factor (δ) due to primary collision of the evaporation flow in Table 2. Corresponding increment in the forward modelled intensities (β_{sim}) in various spectral lines are given in Table 4. Similar to the definition of density increment factor, the intensity increment factor (β_{sim}) is also defined as the ratio of intensities at the loop top followed by the primary collision and to the ambient coronal intensity.

The intensity increment factor depends on the temperature of the loop top and densities. As density increment factor (δ) increases with input heat(Table 2), we obtain larger β_{sim} for all spectral lines (Table 4). So in all times, the density become most important in increasing loop top

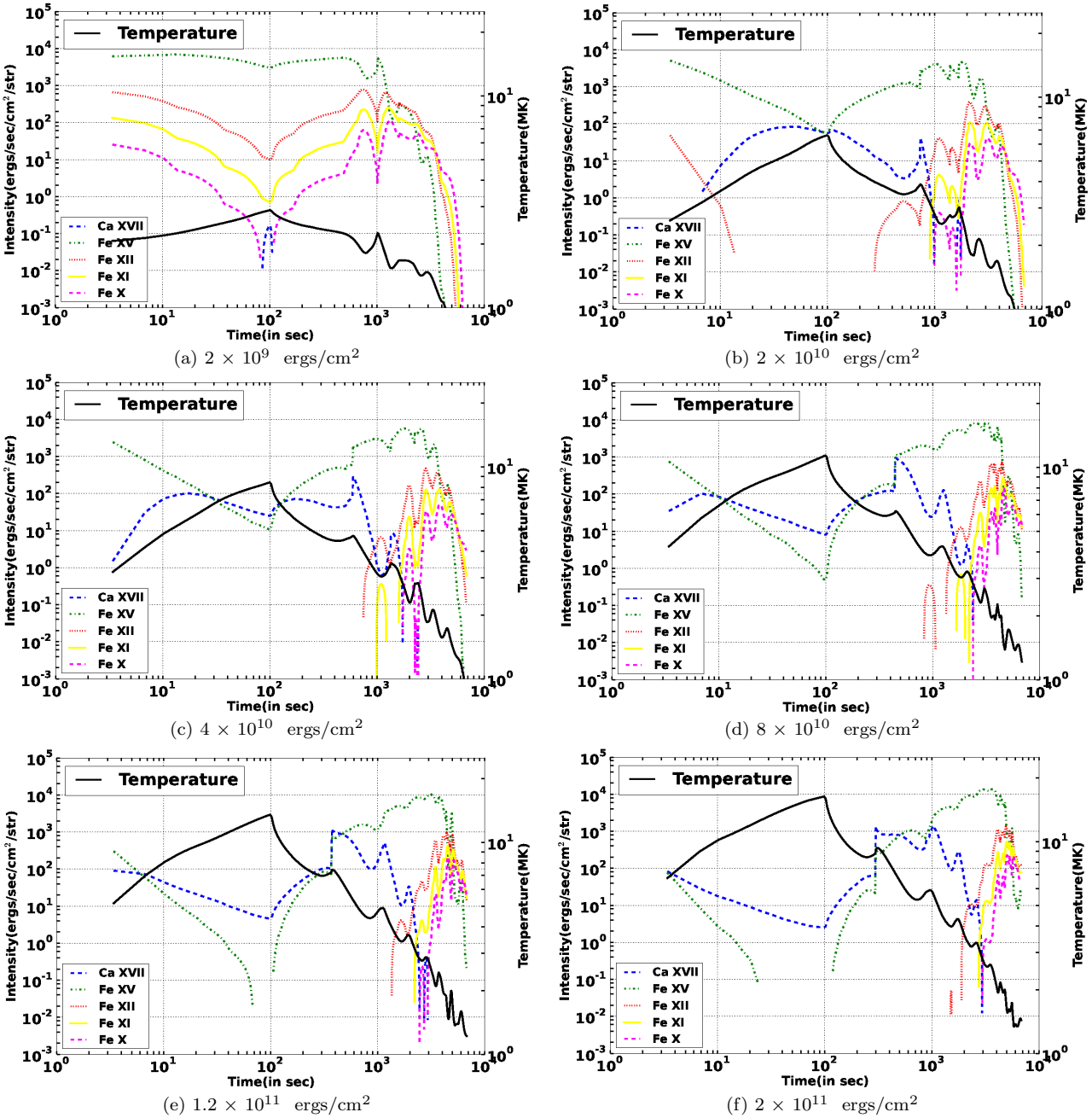

(a) 2×10^9 ergs/cm^2 (b) 2×10^{10} ergs/cm^2

(c) 4×10^{10} ergs/cm^2 (d) 8×10^{10} ergs/cm^2

(e) 1.2×10^{11} ergs/cm^2 (f) 2×10^{11} ergs/cm^2

FIG. 10.— The panel shows the plots of the intensity variation of the loop top with time for different spectral lines along with the temperature of the loop top.

intensity at the time of primary collision. The temperature of the loop top also decides the intensity increment or decrement as seen in Fig 10 depending on the position on the contribution function (Fig 8).

As can be seen from the table, the loop top temperature can reach up to $\sim$ 10 MK for Ca XVII for highest heating. It created the maximum intensity increment of about a factor of 4.4 for Ca XVII. The typical β_{sim} is in the range $\sim$ $1.5 - 3.5$, considering all heating strengths and are close to brightness factor in observation β_{obs} (Table 1). But among all heating inputs, the 8.0×10^{10} ergs cm^{-2} input heat case's loop top increment β_{sim} shows the closest resemblance with the β_{obs} for all spectral lines, except Fe XI. The case of 1.2×10^{11} ergs cm^{-2} is closest to Fe XI. Hotter lines produces larger increments β_{sim} than cooler lines and it increases as input heat increases. In Table 1, this trend does show up from Fe XIII to Ca XVII. In simulations the Fe XV line (Fig. 10, dashed green curve) is dominant for all heating strengths in post-flare times, which is in agreement with the loop top intensity of the observation (Table 1). We note here that there may not be any one-to-one correlation between the observations and forward modelled results. This could be due to the limitations of the simulations and forward modelling. In the simulations, the dynamics corresponding to one loop strand is being studied, whereas in simulations there will be a collection of

TABLE 4
The factor of increment (β_{sim}) in the modelled EIS intensities for various spectral lines for different heating strengths along with the temperature of the loop top.

$H_f \times 10^9$ (ergs cm^{-2})	Fe X	Fe XI	Fe XII	Fe XV	Ca XVII	T_{top} (MK)
2.0	1.15	1.22	1.30	1.64	2.59	1.97
20.0	1.52	1.55	1.60	1.76	2.12	3.49
40.0	1.67	1.55	1.61	1.76	1.94	4.73
80.0	3.20	2.81	2.77	2.81	2.84	6.48
120.0	3.24	1.64	3.31	3.38	3.42	7.61
200.0	5.06	6.45	2.79	3.83	4.42	9.43

strands going through heating and cooling phases simultaneously.

5. SUMMARY AND DISCUSSION

In this paper we have addressed the long standing problem of localised loop top brightening in post flare loops observed in soft X-ray and EUV. We performed a 1D hydrodynamic simulation and forward modelled the intensities in a few spectral lines (see Table 3) observed by EIS. Our results show that the external heating applied at the loop top produces evaporations flows form chromosphere (Fig. 6 & 7). These flows collide at the loop top and enhance the density at the top. This can be clearly seen as increase in the intensities in various spectral lines (Fig. 10). This idea of density enhancement in coronal loops due to chromospheric evaporation is also supported in recent studies such as Takasao et al. (2015) and reference therein. Moreover, once the heating is switched-off, the temperature of the loop top drops sharply due to enhanced radiative cooling. The decline in temperature is larger for stronger heating cases. This is essentially due to the fact that evaporation flows are stronger bringing more mass in the loops thereby increasing the density. We find that temperature of the loop top is important parameter which determines loop top intensity in post flare times. However, the density increments δ (see Table 2) are also proportional to the strength of loop top intensities (Table 4). The intensity increments (β_{sim}) at the time of primary collision are close to observations β_{obs} (Table 1). Our forward modelling shows that Fe XV to the strongest lines for all the heating strengths in the post flare loops. This is consistent with the observations provided by Hara et al. (2008) as shown in Table 1. In post flare times, the cooler spectral lines Fe XII,Fe XI and Fe X appears in the decreasing order of their formation temperatures.

Finally, we conclude that larger external heating produces stronger the evaporation and therefore, creates stronger the loop top brightening in hotter lines. Therefore, the post flare loops formed in higher energetic flare cases will appear brighter. We know that most of the strong flares are observed from complex magnetic regions, for example active regions. However, the low energy flares are often observed from quiescent part of sun's disk. In these cases, a post flare loop formed due to flare eruption of a subsequent CMEs may not be bright enough to be observed. Further investigations regarding effects of various parameters such as heating locations, geometry of the loops as well the length and cross sections are required and is under progress. In addition, more observational study are required to provide quantitative constrains on the relative brightening in different spectral lines.

We thank the referee for careful reading and providing the constructive comments. RS acknowledges the support of Dr Divya Oberoi, NCRA-TIFR, Pune. DT and AG acknowledges the Max-Planck Partner Group of MPS at IUCAA. Hinode is a Japanese mission developed and launched by ISAS/ JAXA, collaborating with NAOJ as a domestic partner, NASA and STFC (UK) as international partners. Scientific operation of the Hinode mission is conducted by the Hinode science team organized at ISAS/JAXA. This team mainly consists of scientists from institutes in the partner countries. Support for the post-launch operation is provided by JAXA and NAOJ (Japan), STFC (UK), NASA, ESA, and NSC (Norway). CHIANTI is a collaborative project involving George Mason University, the University of Michigan (USA) and the University of Cambridge (UK). The authors acknowledge the CANS (Coordinated Astronomical Numerical Software).

REFERENCES

Acton, L. W., Feldman, U., Bruner, M. E., et al. 1992, PASJ, 44, L71
Chen, H., Zhang, J., Ma, S., et al. 2015, ApJ, 808, L24
Cheng, C.-C., Tandberg-Hanssen, E., & Smith, Jr., J. B. 1980, Sol. Phys., 67, 259
Dere, K. P., Landi, E., Mason, H. E., Monsignori Fossi, B. C., & Young, P. R. 1997, A&AS, 125, 149
Feldman, U. 1992, Phys. Scr, 46, 202
Forbes, T. G., & Acton, L. W. 1996, ApJ, 459, 330
Golub, L., Bookbinder, J., Deluca, E., et al. 1999, Physics of Plasmas, 6, 2205
Handy, B. N., Acton, L. W., Kankelborg, C. C., et al. 1999, Sol. Phys., 187, 229
Hara, H., Watanabe, T., Matsuzaki, K., et al. 2008, Publications of the Astronomical Society of Japan, 60, 275
Hori, K., Yokoyama, T., Kosugi, T., & Shibata, K. 1997, ApJ, 489, 426
Howard, T. A., & Harrison, R. A. 2013, Sol. Phys., 285, 269
Kosugi, T., Makishima, K., Murakami, T., et al. 1991, Sol. Phys., 136, 17
Landi, E., Young, P. R., Dere, K. P., Del Zanna, G., & Mason, H. E. 2013, ApJ, 763, 86
Longcope, D. W., & Guidoni, S. E. 2011, ApJ, 740, 73
Longcope, D. W., Guidoni, S. E., & Linton, M. G. 2009, ApJ, 690, L18
Ma, S., Attrill, G. D. R., Golub, L., & Lin, J. 2010, ApJ, 722, 289
Masuda, S., Kosugi, T., Hara, H., Tsuneta, S., & Ogawara, Y. 1994, Nature, 371, 495
Patsourakos, S., Antiochos, S. K., & Klimchuk, J. A. 2004, ApJ, 614, 1022
Priest, E. R., & Forbes, T. G. 2002, A&A Rev., 10, 313
Reeves, K. K., Warren, H. P., & Forbes, T. G. 2007, ApJ, 668, 1210
Shibata, K., & Magara, T. 2011, Living Reviews in Solar Physics, 8, 6
Sun, X., Bobra, M. G., Hoeksema, J. T., et al. 2015, ApJ, 804, L28
Takasao, S., Matsumoto, T., Nakamura, N., & Shibata, K. 2015, ApJ, 805, 135
Tripathi, D., Bothmer, V., & Cremades, H. 2004, A&A, 422, 337
Tsuneta, S. 1996, ApJ, 456, 840
Tsuneta, S., Acton, L., Bruner, M., et al. 1991, Sol. Phys., 136, 37

Warren, H., & Doschek, G. 2006, in Bulletin of the American Astronomical Society, Vol. 38, AAS/Solar Physics Division Meeting #37, 253
Warren, H. P. 2000, ApJ, 536, L105
Warren, H. P., Bookbinder, J. A., Forbes, T. G., et al. 1999, ApJ, 527, L121
Warren, H. P., & Reeves, K. K. 2001, ApJ, 554, L103
Widing, K., & Hiei, E. 1984, ApJ, 281, 426
Yokoyama, T., & Shibata, K. 2001, ApJ, 549, 1160